2018

Thermal-Hydraulic Optimization of Fan-Supplied Tube-Fin Evaporators for Frosting Conditions Aiming at Minimum Energy Consumption

Rafael Ribeiro
Federal University of Parana, Brazil, rafasimrib@gmail.com

Christian Hermes
POLO Labs, Federal University of Santa Catarina, Brazil, hermes@polo.ufsc.br

Diogo Lôndero da Silva
Federal University of Santa Catarina, diogo.londero@ufsc.br

Thermal-Hydraulic Optimization of Fan-Supplied Tube-Fin Evaporators for Frosting Conditions Aiming at Minimum Energy Consumption

Rafael S. RIBEIRO [1], Christian J. L. HERMES [2,*], Diogo L. Da SILVA [3]

[1] Post-Graduation Program in Mechanical Engineering, Federal University of Paraná
81531990, Curitiba, PR, Brazil

[2] POLO Research Laboratories, Department of Mechanical Engineering, Federal University of Santa Catarina
88040900, Florianópolis, SC, Brazil

[3] Laboratory of Vehicular Refrigeration, Department of Mobility Engineering, Federal University of Santa Catarina,
89219600 Joinville, SC, Brazil

[*] Corresponding author: hermes@polo.ufsc.br

ABSTRACT

This work is aimed at the optimal design (i.e. number of transversal and longitudinal tube rows, number of fins) of fan-supplied tube-fin evaporators for light commercial refrigeration applications operating under frosting conditions. Quasi-steady-state algebraic models were put forward for the refrigeration cycle and its components for computing not only the cooling capacity depletion due to the evaporator frosting over time, but also the changes experienced by the evaporating temperature and its effect on the compressor power. Transient, unsteady-state algebraic models were also advanced to account for the temperature and humidity variations inside the refrigerated compartment, and so the compressor runtime. The optimization exercise aiming at system-level energy consumption minimization revealed that, when the evaporator volume and width are held constrained, the lowest energy consumption was achieved for evaporators with evaporators with (3×6), (4×4) and (6×3) (transversal × longitudinal tubes), suggesting that the geometry is robust regarding the evaporator aspect ratio for fan-constrained conditions.

1. INTRODUCTION

According to a recent information note from the International Institute of Refrigeration (Coulomb et al., 2015), there are nearly 3 billion refrigeration, air conditioning and heat pump systems in operation worldwide, consuming by 17% of the overall electricity produced in the globe, which means that 440 kW/year/capita are used for refrigeration purposes. In the realm of the tertiary sector, IIR estimates 90 million commercial refrigerating appliances on the market which respond for roughly 15% of the overall energy consumption attributed to refrigeration.

Most light commercial refrigerators in operation comprises two fan-supplied tube-fin heat exchangers (evaporator and condenser), a hermetic reciprocating compressor, and a capillary tube. Additional components such as a pre-condenser and an internal heat exchanger are also employed. In such applications, the evaporator generally operates at freezing temperatures, a condition favorable to frost build-up over the coil, depleting the cooling capacity because of two concurrent effects namely, the low thermal conductivity of the frost layer, and the reduced air flow passage (Stoecker, 1957) thus requiring longer compressor cycles (i.e., a higher energy input) to accomplish the same cooling effect (Bejan, 1994).

A proper evaporator design for frosting conditions must account for geometric (tubes, fins, heater, fan) and operating (air and coil temperatures, air humidity, defrost cycle) parameters, which not only affect the heat and mass transfer rates, but also the frosting process. To predict the frost accretion on tube-fin evaporators, different simulation models have been advanced (Chen et al., 2003; Yang et al., 2006; Huang et al., 2008; Da Silva et al., 2011b; Padhmanabhan et al., 2011; Ye et al., 2013; and Popovac et al., 2015). Notwithstanding, most of them were not focused on the optimization of the system performance.

Zakrzewski (1984) assessed, by means of a simplified modelling approach, the effect of the thermal resistance due to the frost layer on the cooling capacity depletion over time, noting that there does exist an optimal time between two defrost operations which maximizes the average cooling capacity. Later, Machielsen and Kerschbaumer (1989) improved Zakrzewski's approach, proposing two dimensionless groups (one related to the effective cooling capacity during a complete cycle of operation, and the other to the average energy required to carry out the defrost process), which allowed the determination of the optimum operating time for defrosting. Radcenco et al. (1995) then proposed a system-level optimization to account for the refrigerator performance, reporting an optimal operating time that minimizes the inverse of the system COP, adopted as the figure-of-merit. Recently, Da Silva and Hermes (2018) assessed the defrost cycle of fan-supplied tube-fin evaporators using new defrost data, confirming Zakrzewski's conclusions that there exists an optimal runtime that maximizes the evaporator performance.

Despite the efforts spent in optimizing the defrost cycle, there is a lack in the literature related to the optimal design of the evaporator geometry constrained by a fan-supplied air stream when operating under frosting conditions. To fill this gap, Ribeiro and Hermes (2014) advanced a fully algebraic model to simulate the thermal-hydraulic behavior of fan-supplied tube-fin evaporators running under frosting conditions, which was able to predict the capacity depletion caused by the air flow rate reduction due to the frost blocking, and the augmentation in the heat transfer resistance due to the reduced thermal conductivity of the frost layer. Geometric optimization of the evaporator geometry (number of transversal and longitudinal tubes, number of fins) aiming at minimum entropy generation at the evaporator level were performed, when it was observed that high aspect ratio evaporator designs led to lower rates of entropy generation, although demanding more frequent defrost operations.

The present paper advances the study initiated in 2014, extending the domain of the analysis from the component-level (i.e., the entropy generation in the evaporator) to the system-level (i.e., the amount of energy consumed by the entire refrigerator), thus including the compressor, the fan and the defrost heater into the analysis. For this purpose, the evaporator model developed by Ribeiro and Hermes (2014) was conflated to a quasi-steady-state cycle simulation model (Borges et al., 2011), to account for the changes experienced by the evaporating temperature due to evaporator frosting, and also to a transient cabinet model to assess the temperature and humidity variations inside the refrigerated compartment, thus bringing the compressor runtime into the analysis. A thermodynamic optimization exercise was then carried out based on the total amount of energy consumed.

2. MATHEMATICAL MODEL

The refrigeration system under analysis is a 200-can beverage cooler. To account for different phenomena that take place in all of the system components, the mathematical model is comprised of submodels, namely (i) evaporator heat and mass transfer, (ii) frost build-up, (iii) refrigeration cycle, and (iv) refrigerated compartment.

2.1 Heat and Mass Transfer

Basically, the heat and mass transfer submodel follows the approach introduced in [18], where the surface temperature of the evaporator was assumed to be uniform over the coil. The air flow is assumed one-dimensional, and the air temperature and humidity variations are calculated from energy and mass balances, respectively. From the boundary layer analogy, $\rho D Sh = k Nu / c_p Le^{2/3}$, where $Le \approx 1$ is the Lewis number, Nu and Sh are the Nusselt and Sherwood numbers, respectively, being both based on the hydraulic diameter, $Dh = 4LA_c/A_s$, the sensible heat, Q_{sen}, and latent heat transfer rates, Q_{lat}, can be calculated from:

$$\frac{Q_{sen}}{c_{p,air}\left(T_{cab} - T_{fs}\right)} = \frac{Q_{lat}}{i_{sv}\left(\omega_{cab} - \omega_{fs}\right)} = \rho V_{air}\left(1 - \exp\left(-St\frac{A_s}{A_c}\right)\right) \tag{1}$$

where $St = Nu/RePr$ is the Stanton number, $Re = \rho V_{air} D_h / \mu A_c$ is the Reynolds number, Pr the Prandtl number, T_{fs} and $\omega_{fs} = \omega_{sat}(T_{fs})$ are the temperature and humidity conditions on the frost surface, A_s is the heat and mass transfer surface (see eq. 6), A_c is the minimum free flow passage (see eq. 5), L is the heat exchanger length in the flow direction, D is the water vapor diffusivity in air, k and $c_{p,air}$ are, respectively, the thermal conductivity and the specific heat of the moist air, and i_{sv} is the latent heat of sublimation. The air-side pressure drop, on the other hand, is calculated from:

$$\Delta p = p_i - p_o = \frac{C_f \rho}{2}\left(\frac{V_{air}}{A_c}\right)^2 \frac{A_s}{A_c} \tag{2}$$

where the air flow rate $V_{air}=V_{air}(\Delta p)$ is obtained from the fan characteristic curve, modelled according to the following equation, $\Delta p=\Delta p_0(1-(V/V_{max})^2)$, where Δp_0 and V_{max} are the pressure head (100 Pa) and the maximum air flow rate (200 m^3/h) delivered at shut-off and free-delivery conditions, respectively. The Stanton number, St, and the Fanning friction factor, C_f, are calculated by means of empirical correlations, $StPr^{2/3}=a_0Re^{a1}\phi^{a2}$ and $C_f=b_0Re^{b1}\phi^{b2}$, being both fitted to experimental data from Da Silva et al. (2011a), where ϕ is the finning factor, i.e. the ratio between to total heat transfer surface (tubes and fins) to the heat transfer surface due to the tubes only. The coefficients are as follows: $a_0=33$, $a_1=-0.82$, $a_2=-1.23$, $b_0=256$, $b_1=-0.82$ and $b_2=-1.36$.

The thermodynamic analysis was initially performed based on the rate of entropy generated externally on the evaporator coil, calculated as follows

$$S_{g,ext} = \frac{Q_{sen}}{T_{fs}}\frac{\Delta T}{T_{lm}} + R_v\frac{Q_{lat}}{i_{sv}}\frac{\Delta\omega}{\omega_{lm}} + \frac{V_{air}\Delta p}{T_{lm}} \tag{3}$$

The first term in the right-hand side stands for the entropy generation due to heat transfer, the second term is related to the mass transfer, and the third term to the pumping power. The term related to the conjugate heat and mass transfer was disregarded as it plays a minor role on the total rate of entropy generation. In eq. (3), the temperature and humidity differences, and the mean temperature and humidity are calculated from logarithmic means.

2.2 Frost Growth

The frost growth and densification submodel is based on the algebraic approach proposed by Hermes (2012), which was originally developed for horizontal flat plates, and adapted here for the tube-fin heat exchanger geometry by considering the hydraulic diameter as the characteristic scale instead of the plate length. Thus, the frost layer thickness, δ_{fs}, can be calculated from:

$$\frac{\delta_{fs}}{D_h} = \frac{1}{2}\left(\left(\left(\frac{k_{fo}}{k}\frac{Ja}{Nu(1+Ja)}\right)^2 + 4\left(\omega_{lm}-\omega_{sat}(T_{evp})\right)\frac{k_{fo}}{k}\frac{JaFo}{1+Ja}\right)^{1/2} - \frac{k_{fo}}{k}\frac{Ja}{Nu(1+Ja)}\right) \tag{4}$$

where $Fo=k_f t/\rho_f c_p D_h^2$ is the modified Fourier number, $Ja=c_{p,air}(T_{dew}-T_{evp})/(\omega_{lm}-\omega_{sat})i_{sv}$ is the modified Jakob number, and $Nu=StRePr$ is the Nusselt number. It is worth of note that eq. (4) conveys the $\delta_{fs}\sim\sqrt{t}$ scale into the evaporator frosting problem, which is a typical behavior of diffusive-dominant processes. The frost density, $\rho_f=c_0\exp(c_1T_{fs})$, and the thermal conductivity, $k_f=k_{fo}+\beta\rho_f$, were calculated from empirical correlations. The coefficients $c_0=53$ and $c_1=-0.159$ were adjusted by Ribeiro and Hermes (2014), while $k_{fo}=0.1312$ and $\beta=0.0003$ were obtained from Hermes (2012). The frosted heat exchanger geometry (Ac, As) is calculated from (see Fig. 1):

$$A_c = WH - N_{tr}D_{eff}\left(W-\delta_{eff}N_{fin}\right) - N_{fin}\delta_{eff}H \tag{5}$$

$$A_s = \pi D_{eff}\left(W-\delta_{eff}N_{fin}\right)N_{tr}N_{lo} + 2N_{fin}\left(HL - \tfrac{1}{4}\pi D_{eff}^2 N_{tr}N_{lo}\right) \tag{6}$$

where $D_{eff}=D_t+2\delta_{fs}$, $\delta_{eff}=\delta_{fin}+2\delta_{fs}$, D_t is external diameter of the tube, δ_{fin} and N_{fin} are the thickness and the number of fins, respectively, and N_{tr} and N_{lo} are the numbers of tubes in the transversal and longitudinal directions, respectively, which define the aspect ratio of the heat exchanger, i.e. H (N_{tr}) × L (N_{lo}), as illustrated in Fig 2. The model validation exercise for the frosting evaporator was performed in Ribeiro and Hermes (2014). Figure 3 compares, with the experimental counterparts obtained from Silva et al. (2011a), the time evolution of the calculated cooling capacity, whereas Fig. 4 compares the air flow rate, where one can note that the model is able to follow the experimental trends quite satisfactorily, especially after the early transients (i.e. from 10 min on), where the frost formation effects are more perceptible. It can be also noted that the heat exchanger with a high number of fins provide a higher cooling capacity, which is due to the higher heat transfer (finned) surface, while operating under lower air flow rates because of the increased pressure drop.

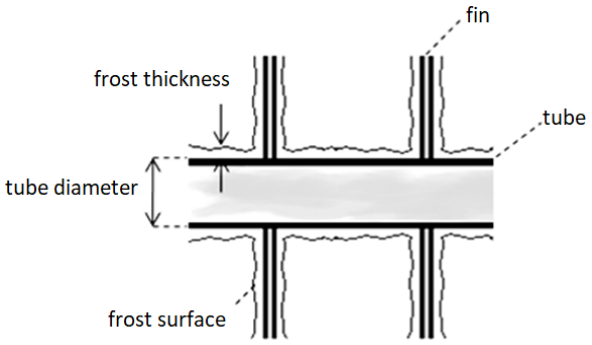

Figure 1: Front-view of frost blocking taking place in a small part of the evaporator face area

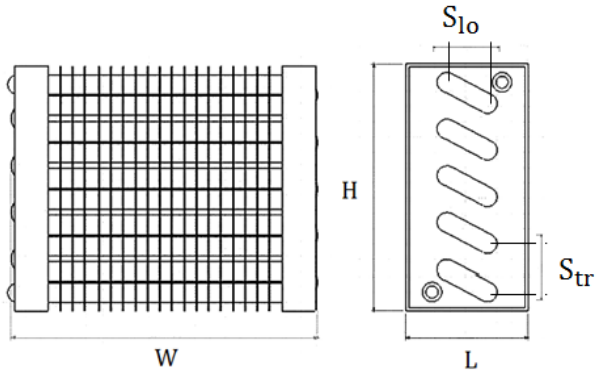

Figure 2: Schematic representation of the evaporator geometry

2.3 Refrigeration Cycle

The system under analysis is comprised of a vapor compression cycle with a liquid-to-suction heat exchanger running with R-134a, as depicted in Fig. 5. Assuming a 100%-effective internal heat exchanger (Hermes, 2013), and also that the vapor refrigerant behaves as an ideal gas, the compression power and the cooling capacity are calculated as follows

$$W_{cmp} = \frac{\eta_v}{\eta_g} V_{cmp} P_{evp} \frac{\gamma}{\gamma - 1} \left(\left(\frac{P_{cnd}}{P_{evp}} \right)^{1-1/\gamma} - 1 \right) \tag{7}$$

$$Q_{evp} = \eta_v \frac{V_{cmp} P_{evp}}{R T_{cnd}} \left(h_{vap}^{evp} - h_{liq}^{cnd} + c_{p,vap}^{evp} \left(T_{cnd} - T_{evp} \right) \right) \tag{8}$$

where V_{cmp} is the piston displacement in [m^3/s], R and γ are the gas constant and the isentropic exponent for the R-134a, respectively, η_v and η_g are the compressor volumetric and global efficiencies, with $\eta_v/\eta_g \approx 1$, and the superscripts evp and cnd stand for the saturated conditions at the evaporating, T_{evp}, and condensing, T_{cnd}, temperatures, respectively. The working pressures P_{evp} and P_{cnd} are obtained from the evaporating and condensing temperatures, respectively, as the model assumed the vapor quality to be 0 and 1 at the condenser and the evaporator outlet, respectively. For a fixed cooling capacity, the evaporating temperature must be calculated iteratively from eq. (8) by making $Q_{evp}=Q_{sen}+Q_{lat}$. In this work, the condensing temperature was held fixed at 40ºC.

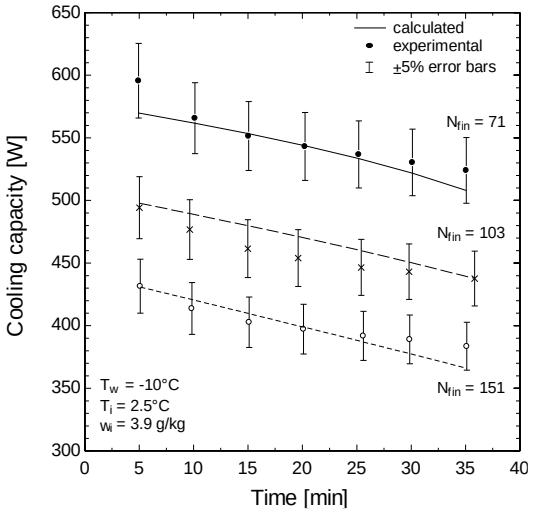

Figure 3: Comparison between calculated and experimental cooling capacities for 71, 103 and 151 fins

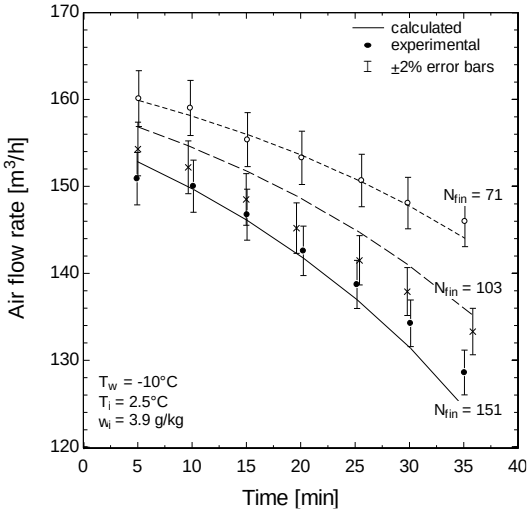

Figure 4: Comparison between calculated and experimental air flow rates for 71, 103 and 151 fins

The rate of entropy generated internally in the refrigeration cycle is calculated from an overall entropy balance in the refrigerator operating between the condensing, Tcnd, and the evaporating, Tevp, temperatures:

$$S_{g,int} = \frac{Q_{evp}}{T_{cnd}}\left(COP^{-1} - COP_{int,rev}^{-1}\right) \tag{9}$$

where $COP=Q_{evp}/W_{cmp}$ is the coefficient of performance of the refrigeration system, whereas the $COP_{int,rev}=T_{evp}/(T_{cnd}-T_{evp})$ is the coefficient of performance of an endoreversible refrigeration cycle.

2.4 Refrigerated Compartments

The refrigerated compartment submodel is required for feeding the evaporator submodel with more realistic boundary conditions, as the compartment temperature and humidity vary with time as the refrigeration system is controlled by means of an on-off pattern. The cabinet submodel was then obtained from energy and mass balances through the control volumes indicated in Fig. 5, whose analytical solution over the time-step (Δt) yields the following algebraic expressions (Ribeiro, 2016):

$$T_{cab}(t+\Delta t) = T_{ref}(t) - \left(T_{ref}(t) - T_{cab}(t)\right)\exp\left(-\frac{\left(\rho V c_p\right)_{air} + UA_{cab} + K_{inf}c_{p,air}}{\left(Mc_p\right)_{load}}\Delta t\right) \tag{10}$$

$$\omega_{cab}(t+\Delta t) = \omega_{ref}(t) - \left(\omega_{ref}(t) - \omega_{cab}(t)\right)\exp\left(-\frac{\left(\rho V\right)_{air} + K_{inf}}{M_{air}}\Delta t\right) \tag{11}$$

where $T_{ref}(t)$ and $\omega_{ref}(t)$ are calculated from:

$$T_{ref}(t) = \frac{\left(\rho V c_p\right)_{air} T_{out}(t) + UA_{cab}T_{surr} + K_{inf}c_{p,air}T_{surr} + W_{fan} + W_{def}\left(1-\eta_{def}\right)}{\left(\rho V c_p\right)_{air} + UA_{cab} + K_{inf}c_{p,air}} \tag{12}$$

$$\omega_{ref}(t) = \frac{\left(\rho V\right)_{air}\omega_{out}(t) + K_{inf}\omega_{surr}}{\left(\rho V\right)_{air} + K_{inf}} \tag{13}$$

where UA_{cab} is the thermal conductance of the cabinet walls, K_{inf} refers to the external air infiltration, W_{fan} is the power consumed by the fan, while W_{def} is the heat generated by the defrost heater, and η_{def} is the defrost efficiency.

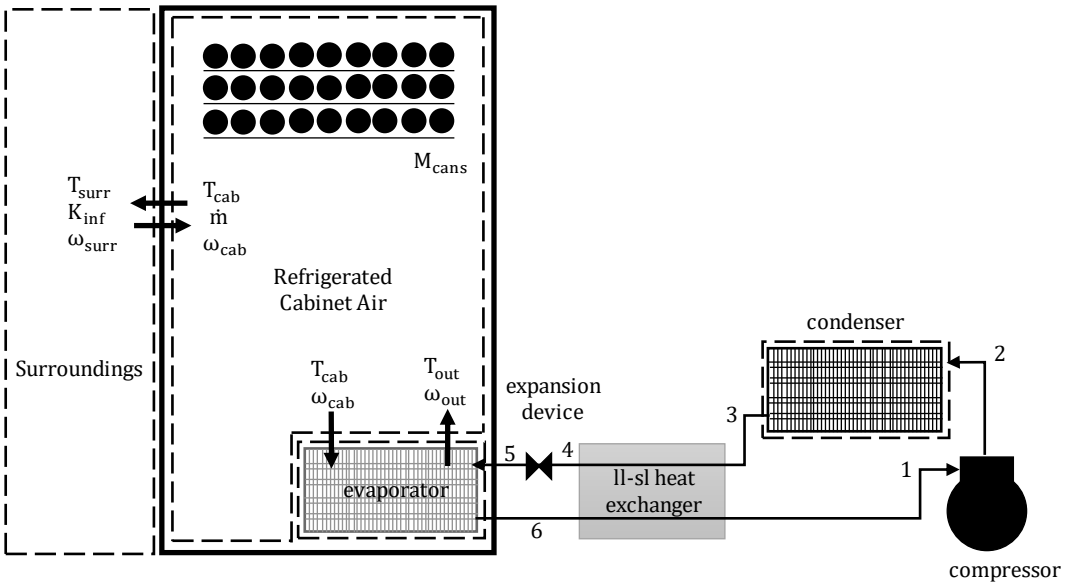

Figure 5: Schematic representation of the refrigerated compartment, and the refrigeration loop

The defrosting time is calculated from

$$t_{def} = \frac{i_{sl}}{\eta_{def} W_{def}} \int_{t}^{t+\tau} \frac{Q_{lat}}{i_{sv}} dt \tag{14}$$

where i_{sl} is the latent heat of melting, whereas i_{sv} is the latent heat of sublimation, and τ is the time between two defrost operations in a row, which take place whenever the frost blocks 70% of the evaporator face area, i.e. $A_c/WH<0.3$. The cabinet is loaded with 200 cans of 350 ml each whose thermophysical properties were assumed to be those of pure water. The refrigeration system is on-off controlled to keep the cabinet at an average temperature of 5ºC with ±2.5ºC of variation. At the initial time, the cabinet and its contents are all at 5ºC, with saturated relative humidity. The surroundings conditions are 32ºC, 80% RH.

2.5 Solution Scheme

The equation set is fully comprised of time-dependent algebraic non-linear equations which have been solved simultaneously for each time-step by means of the Newton-Raphson technique (Stoecker, 1989). The optimization exercise was carried out by an exhaustive search by varying two out of the three the geometric characteristics of the heat exchanger, i.e. N_{fin}, N_{tr} and N_{lo}, while the third is held fixed. The two-dimensional response surface was then conflated to the constant volume constraint to limit the loci of optima. In case non-integer geometries, i.e. N_{fin}, N_{tr} and N_{lo}, sub-optimum solutions have been considered. More detailed information can be found in Ribeiro (2016).

3. RESULTS

The numbers of transversal and longitudinal tubes together with the number of fins were taken as the independent parameters for the optimization exercise, whereas the tube and fin spacings were held fixed. Therefore, by changing the number of tubes and fins, different evaporator envelopes (height × length × width) could be assessed, as depicted in Fig. 6. Initially, the optimization exercise was carried out for the evaporator only – i.e. decoupled from the refrigerator – so that the inlet air conditions were held fixed at 5°C (dry-bulb temperature) and 3.9 g/kg (humidity ratio). The objective function used in this first optimization exercise was the time-averaged rate of entropy generation, calculated from:

$$S_{g,avg} = \frac{1}{t_{on}} \int_{0}^{t_{on}} S_g dt \tag{15}$$

where S_g is calculated from Eq. (3), and ton is the runtime until the evaporator free flow passage (the ratio between the free flow area and the face area, A_c/WH) is below 30%. Note that the blockage of 70% of the face area was chosen as the defrost criterion in all optimization analyses reported here. An average cooling capacity of 450 W was also imposed to the model so that the evaporating temperature was free to float during the optimization exercise.

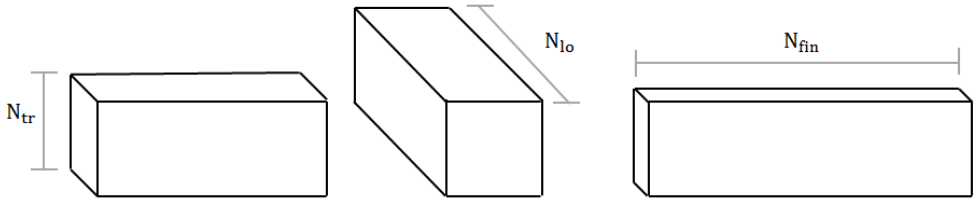

Figure 6: Prospective design configurations in a volume-constrained optimization exercise

Figure 7 illustrates the results for the case where the number of fins (i.e. evaporator width, N_{fin}=103) is the only geometric parameter held fixed. The analysis points out an entropy generation minimization path towards higher face areas and heat exchanger lengths, thus contradicting the predictions reported by Ribeiro and Hermes (2014), which in turn pointed out slender (high aspect ratio) designs as the ones which generate the minimum amount of entropy. It is worth of note that, in the author's previous publication (Ribeiro and Hermes, 2014), where it reads 'dimensionless entropy generation rate', it should read, instead, 'the product of the dimensionless entropy generation

rate by the heat transfer area'. Such a figure-of-merit (not the rate of entropy generation) led to a high aspect ratio heat exchanger design for frosting conditions. In the case when both the evaporator volume and height were set as design constraints (3-liter, N_{tr}=6), a region of minimum entropy generation was observed, as illustrated in Fig. 8, where the bulleted-dashed-line indicates the 3-liter volume constraint. Marching along the constraint from the bottom corner up, one can find out the optimal figures for the number of fins (N_{fin}≈75) and the number of longitudinal tubes (N_{lo}≈4).

The influence of the refrigeration system on the evaporator behavior, which affects the evaporating temperature (in addition to the average cooling demand imposed to the model) is at the aim of the analysis reported in Fig. 10. On the one hand, the coil temperature was once again let free to vary, but in a stiffer fashion than before as it is now driven not only by the air-side heat and mass transfer, but also by the refrigeration cycle constraints. The condensing temperature, on the other hand, was held fixed at 40ºC. The air inlet conditions are the same as before (5°C dry-bulb temperature and 3.9 g/kg humidity ratio), whereas the objective function is the time-averaged rate of entropy generation summing up the internal (eq. 9) and external (eq. 3) irreversibilities in eq. (15).

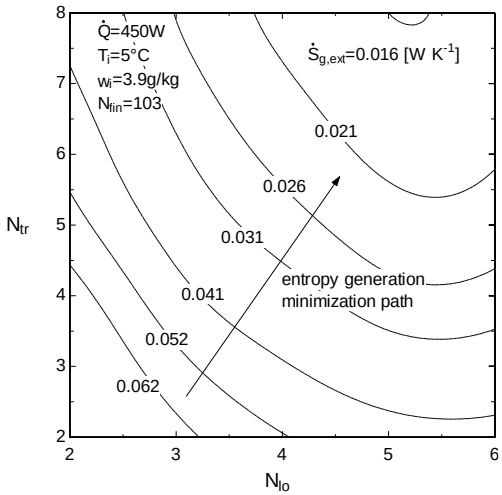

Figure 7: Time-averaged rate of entropy generation minimization path for the evaporator alone

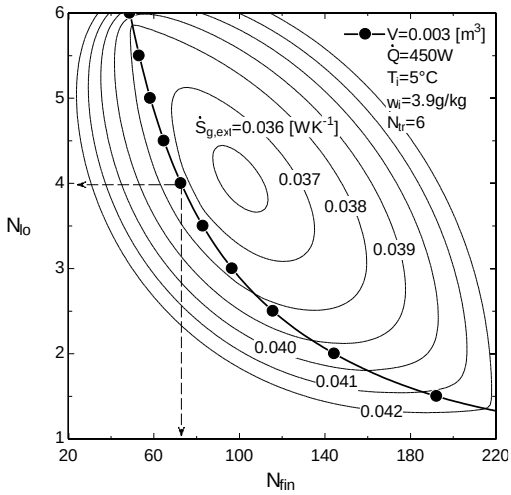

Figure 8: Time-averaged rate of entropy generation considering the external irreversibilities

Figure 9 shows the results obtained for considering once again both the evaporator volume and height as design constraints (3-liter, N_{tr}=6). The average cooling demand was set to 450 W. Results that diverted from the ones from the previous analysis were achieved, with significantly higher figures for the rate of entropy generation in Fig. 9 (in comparison with Fig. 8, as both the internal and external irreversibilities are now being taken into account), and slightly different optimal numbers of fins (≈60) and longitudinal tubes (≈5). Such a behavior can be explained by the variations experienced by the coil temperature, higher for the case when the evaporator was analyzed alone in comparison to the case when it was coupled to the system. In the latter, the heat transfer area must increase to accommodate the frost mass, and also to provide the cooling demand for an evaporating temperature higher than that observed for the evaporator alone.

Nonetheless, it should be noted that the previous analyses, not only that of Figs. 8 and 9, but also those reported in Ribeiro and Hermes (2014) were all carried out for fixed air-side conditions at the evaporator inlet, which is not a realistic assumption for refrigerators running under an on-off control pattern. In addition, the analyses have not taken the defrost process into account, which not only contributes to the total power consumption but also rises the thermal loads inside the refrigerated compartments. Therefore, to compare the performances of different evaporator aspect ratios, a final optimization exercise was carried out considering the whole refrigeration system, with the refrigeration system coupled to the refrigerated compartments. Simulations were carried out over long time periods (~12 h) until the average cooling capacity reached the average cabinet thermal load (which, for all cases, stabilizes at 220 W), as depicted in Fig. 10. In the present analysis, the volume and width were held constrained (under the very same conditions used in the analysis depicted in Fig. 7, i.e. 3-liter, N_{fin}=103), whereas the air conditions at the evaporator inlet and the coil temperature changed over time. Periodic defrost operations also took place every time the

evaporator face area got 70% blocked. The overall energy consumption was taken as the objective function, calculated from the time integration of the total power consumed by the refrigerator during its operation, as follows:

$$EC = \frac{1}{t_{on} + t_{off}} \int_{t_{on}}^{t_{on}+t_{off}} \left(W_{cmp} + W_{fan} + W_{def} \right) dt \tag{16}$$

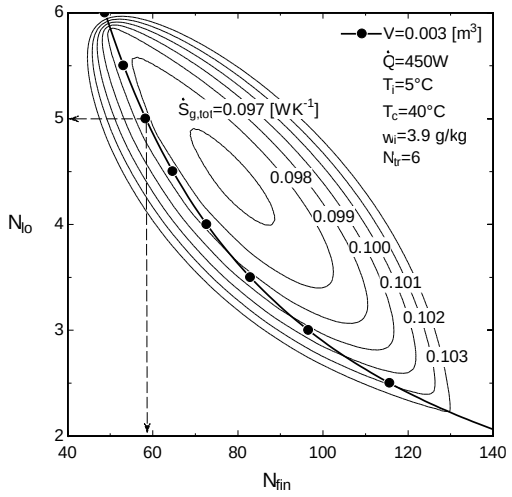

Figure 9: Time-averaged rate of entropy generation considering the internal and external irreversibilities

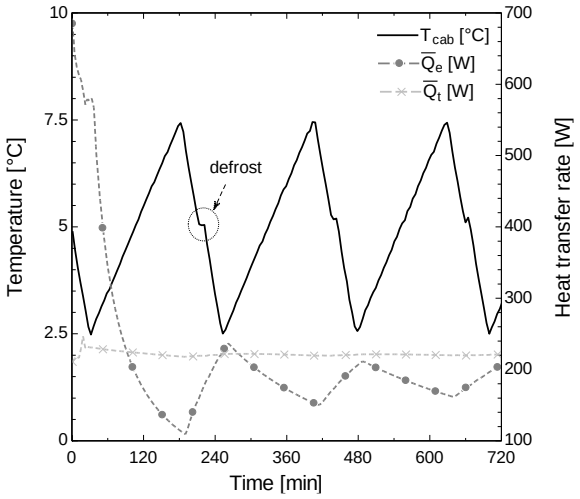

Figure 10: Cycling behavior with the time-averaged cooling capacity and thermal loads

The results for the total energy consumption (which accounts for compressor, fan, and defrost heater power consumption integrated over time) and the runtime to reach steady-state conditions are depicted in Figs. 11 and 12. One can note that the optimization path follows the bulleted-dashed-line which contains the geometries (Ntr, Nlo) that satisfy the volume constraint. One can note in Fig. 11 the parallelism between the energy consumption contours and the volume constraint line, suggesting that configurations with $N_{tr}=N_{lo}=4$, $N_{tr}=6$ and $N_{lo}=3$, or $N_{tr}=3$ and $N_{lo}=6$, come out with similar figures for the total energy consumption (≈129 kWh/month) (see Fig. 11), thus indicating that the system is robust to the evaporator aspect ratio since there is enough heat transfer area to get the job done. Figure 12 reveals that the system runtime showed to be quite insensitive to the evaporator geometry. Such results can be partly explained by the fact that the air flow rate is constrained by the fan characteristics, and partly because of the model limitations, as it considers a uniform frost formation, thus distributing the frost mass evenly over the coil, which is not observed in real evaporators that show thicker frost layers in the first rows (Da Silva et al., 2011b).

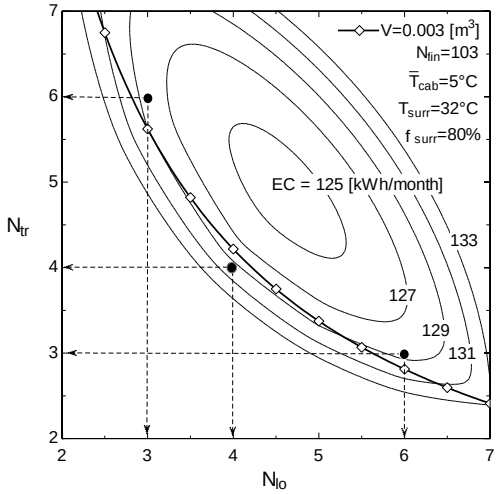

Figure 11: Optimal energy consumption to reach steady-state conditions in case of constrained volume

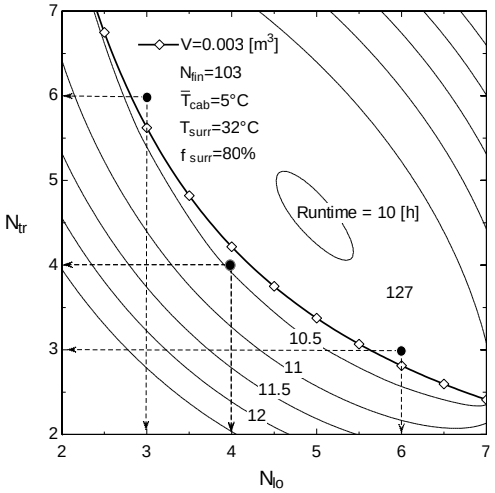

Figure 12: Optimal runtime to reach steady-state conditions in case of constrained volume

4. CONCLUDING REMARKS

Algebraic submodels were proposed and solved together for simulating the effect of the evaporator frosting and defrosting on the total energy consumption of a small-capacity beverage cooler. Two levels of optimization were tested, from the component-level (evaporator only) to the system-level (evaporator coupled to the refrigeration loop and the refrigerated compartment). The optimal configuration obtained for the evaporator alone, i.e. when only the external irreversibilities are considered, differs from the one achieved when the total (internal and external irreversibilities) are accounted for. While the former points out a lower number of longitudinal tubes (N_{lo}=4) and a higher number of fins (N_{fin}≈75) as the best design, the latter leads to N_{lo}=5 and N_{fin}≈60, which is due to the variations experienced by the evaporating temperature, which decreases with the frost build-up. The optimization exercise considering the entire refrigeration system aiming at minimum energy consumption revealed that, when the evaporator volume and width are held constrained, similar energy consumption figures were observed for evaporators with (3×6), (4×4) and (6×3) (transversal tubes × longitudinal tubes). Such a result suggests that, when the fan characteristic curve is constrained, the optimal geometry is robust regarding the aspect ratio. However, it is worth noting that the frost growth model adopted in this work considers a uniform frost formation, thus distributing the frost mass evenly over the evaporator surface, which is not observed in real applications where the frost is more likely to build-up at the first rows due not only to a higher mass transfer coefficient, but also to a higher humidity gradient. Therefore, a slender evaporator configuration, i.e. the (6×3) one, seems to be the best design both in terms of energy performance and robustness to frost clogging, despite being costly if compared to the (4×4) solution.

NOMENCLATURE

Roman

A_c	minimum free flow area [m^2]
A_s	surface area [m^2]
C_f	Fanning friction factor [-]
c_p	specific heat at constant pressure [J $kg^{-1}K^{-1}$]
D	diffusivity of water vapor in air [m^2 s^{-1}]
D_h	hydraulic diameter [m]
Fo	Fourier number [-]
H	height [m]
i_{sl}	latent heat of fusion [J kg^{-1}]
i_{sv}	latent heat of sublimation [J kg^{-1}]
Ja	Jakob number [-]
k	thermal conductivity [W $m^{-1}K^{-1}$]
L	length [m]
Le	Lewis number [-]
m	mass flux [kg_v $m^{-2}s^{-1}$]
N_{fin}	number of fins [-]
N_{lo}	number of longitudinal tube rows [-]
N_{tr}	number of transversal tube rows [-]
Nu	Nusselt number [-]
Q	heat transfer rate [W]
R	gas constant [J $kg^{-1}K^{-1}$]
S_{fin}	fin spacing [m]
S_g	entropy generation rate [W K^{-1}]
Sh	Sherwood number [-]
St	Stanton number [-]
T	temperature [K]
t	time [s]
V_{air}	air flow rate [m^3 s^{-1}]
V_{cmp}	piston displacement [m^3 s^{-1}]
W	width [m]
W_{cmp}	compression power [W]

Greek

ρ	density [kg m^{-3}]
ϕ	finning factor [-]
ω	humidity ratio [-]
γ	isentropic exponent [-]
δ	thickness [m]
τ	runtime between defrost operations [s]

Subscripts

air	moist air
avg	time-averaged
cab	cabinet, evaporator inlet
cmp	compressor
cnd	condenser
eff	effective frosted geometry
evp	evaporator
ext	externally to the cycle
f	frost
fin	fin
fs	frost surface
inf	infiltration
int	internally to the cycle
lat	latent
liq	saturated liquid refrigerant
lm	logarithmic mean
out	evaporator outlet
sat	saturated
sen	sensible
surr	surroundings
t	tube geometry
vap	saturated vapor refrigerant

REFERENCES

Bejan A, Vargas JVC, Lim JS (1994) When to defrost a refrigerator, and when to remove the scale from the heat exchanger of a power plant, *Int. J. Heat Mass Transfer* 37 523-532

Borges BN, Hermes CJL, Goncalves JM, Melo C (2011) Transient Simulation of Household Refrigerators: A Semi-Empirical Quasi-Steady Approach, *Applied Energy* 88 748–754

Chen H, Thomas L, Besant RW (2003) Fan supplied heat exchanger fin performance under frosting conditions, *Int. J. Refrig.* 26 140–149

Coulomb D, Dupont J-L, Pichard A (2015) *The Role of Refrigeration in the Global Economy*, 29th Informatory Note on Refrigeration Technologies, International Institute of Refrigeration, Paris, France

Da Silva DL, Hermes CJL (2018) Optimal defrost cycle for air coolers revisited: A study of fan-supplied tube-fin evaporators, *Int. J. Refrig.* doi:10.1016/i.ijrefrig.2018.02.009

Da Silva DL, Hermes CJL, Melo C (2011a) Experimental study of frost accumulation on fan-supplied tube-fin evaporators, *App. Therm. Eng.* 31 1013-1020

Da Silva DL, Hermes CJL, Melo C (2011b) First-principles simulation of frost accumulation on fan-supplied tube-fin evaporators, *App. Therm. Eng.* 31 2616-2621

Hermes CJL (2012) An analytical solution to the problem of frost growth and densification on flat surfaces, *Int. J. Heat Mass Transfer* 55 7346-7351

Hermes CJL (2013) Alternative evaluation of liquid-to-suction heat exchange in the refrigeration cycle, *Int. J. Refrig.* 36 2219-2227

Huang JM, Hsieh WC, Ke XJ, Wang CC (2008) The effects of frost thickness on the heat transfer of finned tube heat exchanger subject to the combined influence of fan types, *App. Therm. Eng.* 28 28–737

Machielsen CHM, Kerschbaumer HG (1989) Influence of frost formation and defrost on the performance of air coolers: standards and dimensionless coefficients for the system designer, *Int. J. Refrig.* 12 283-290.

Padhmanabhan SK, Fischer DE, Cremaschi L, Moallem E (2011) Modeling non-uniform frost growth on a fin-and-tube heat exchanger, *Int. J. Refrig.* 34 2018-2030

Popovac M, Seichter S, Benovsky P, Fleckl T, Reichl C (2015) Numerical analysis of the frosting performance of the air side of a heat pump, *Int. Congr. Refrig.*, Yokohama, Japan

Radcenco V, Bejan A, Vargas JVC, Lim JS (1995) Two design aspects of defrosting refrigerators, *Int. J. Refrig.* 18 76-86

Ribeiro RS (2016) *Thermodynamic analysis of tube-fin evaporators subjected to frosting conditions*, MEng Thesis, Department of Mechanical Engineering, Federal University of Paraná, Curitiba, PR, Brazil (in Portuguese)

Ribeiro RS, Hermes CJL (2014) Algebraic modeling and thermodynamic design of fan-supplied tube-fin evaporators running under frosting conditions, *App. Therm. Eng.* 70 552-559

Stoecker WF (1957) How frost formation on coils affects refrigeration systems, *Refrigerating Engineering* 65, No. 2

Stoecker WF (1989) *Design of Thermal Systems*, McGraw-Hill, New York, NY, USA

Yang DH, Lee KS, Song S (2006) Modeling for predicting frosting behavior of a fin-tube heat exchanger, *Int. J. Heat Mass Transfer* 49 1472-1479

Ye H-Y, Lee KS (2013) Performance prediction of a fin-and-tube heat exchanger considering air-flow reduction due to the frost accumulation, Int. J. Heat Mass Transfer 67 225-233

Zakrzewski B (1984) Optimal defrost cycle for the air cooler, Int. J. Refrig. 7 41-45

ACKNOWLEDGEMENTS

This study was carried out under the auspices of the Brazilian Government funding agencies CAPES and CNPq.